



## Diffraction by multipoles in a $5d^2$ rhenium double perovskite

S. W. Lovesey <sup>1,2</sup>, D. D. Khalyavin,<sup>1</sup> G. van der Laan <sup>2</sup> and G. J. Nilsen<sup>1</sup>

<sup>1</sup>ISIS Facility, STFC, Didcot, Oxfordshire OX11 0QX, United Kingdom

<sup>2</sup>Diamond Light Source Ltd, Didcot, Oxfordshire OX11 0DE, United Kingdom



(Received 7 December 2020; accepted 8 February 2021; published 19 March 2021)

A recent polarized neutron diffraction experiment on the  $5d^2$  rhenium double perovskite  $\text{Ba}_2\text{YReO}_6$  held at a low temperature uncovered weak magnetic diffraction peaks. Data analysis inferred a significantly reduced Re dipole moment, and long-range order compatible with an antiferromagnetic, noncollinear motif. To interpret the experimental findings, we present a model wave function for Re ions derived from the crystal field potential, Coulomb interaction, and spin-orbit coupling that fully respects the symmetry of the low-temperature ordered state. It is used to calculate in analytic form all multipole moments visible in neutron and resonance enhanced x-ray diffraction. A minimal model consistent with available neutron diffraction data predicts significant multipolar moments up to the hexadecapole and, in particular, a dominant chargelike quadrupole moment. Calculated diffraction patterns embrace single crystal x-ray diffraction at the Re  $L$  edge, and renewed neutron diffraction, to probe the presumed underlying multipolar order.

DOI: [10.1103/PhysRevB.103.104429](https://doi.org/10.1103/PhysRevB.103.104429)

### I. INTRODUCTION

Scattering techniques yield a wealth of knowledge about electronic properties of materials at an atomic level of detail. To begin with, a Bragg diffraction pattern produced by Thomson scattering of x rays is analyzed in terms of spheres of electronic charge arranged on a structure defined by a space group. Space-group forbidden Bragg spots attributed to quadrupole moments produced by departures from spherical distributions of charge are weak, by their very nature. Their intensities can be enhanced by an atomic resonance in what is often called Templeton-Templeton (TT) scattering. Classic examples are sodium bromate and sodium chlorate, which possess the same chirality yet opposite senses of optical rotation [1]. Beyond, Bragg diffraction by a nonmagnetic hexadecapole was observed in ichorlike haematite ( $\alpha\text{-Fe}_2\text{O}_3$ ) [2]. Magnetic octupoles occur in haematite and vanadium sesquioxide ( $\text{V}_2\text{O}_3$ ), for example, and are fully understood [3,4]. Moreover, parity-odd magnetic (Dirac) multipoles have been observed in both materials by x-ray diffraction [5,6]. In addition to the examples of multipoles in the two 3  $d$ -transition metal materials are multipoles observed in diffraction by rare earth and actinide ( $f$  electron) compounds, e.g., neptunium dioxide  $\text{NpO}_2$  [7] and  $\text{URu}_2\text{Si}_2$  [8], and like work is reviewed by Suzuki *et al.* [9]. Neutron diffraction came late to the party with respect to gathering information on higher-order magnetic multipoles, although it is the technique of choice for determining motifs of conventional (axial) magnetic dipoles, beginning with a demonstration by Shull and Smart in 1949 of antiferromagnetic order in NaCl-type MnO below 122 K [10]. Two decades later, Moon, Riste, and Koehler demonstrated advantages of exploiting neutron polarization analysis [11]. Specifically, the technique yields superior statistics on weak magnetic Bragg spots. Recent

examples include the detection of long-range magnetic orders in the pseudogap phases of YBCO and Hg1201 and field-induced magnetization in  $\text{Sr}_2\text{IrO}_4$  [12,13]. Subsequent analyses of the patterns revealed contributions to diffraction by Dirac multipoles in the ceramic superconductors, and  $5d^5$  quadrupoles and octupoles in the iridate [14,15]. Extra knowledge, including moment directions, derived from polarization analysis refines models and, thereby, makes predictions and functional designs ever more reliable [16].

Work reported here is motivated by the observation of a magnetic powder Bragg diffraction pattern for the low-temperature (1.8 K) modification of the rhenate  $\text{Ba}_2\text{YReO}_6$ , which crystalizes in the elpasolite structure [17]. Albeit composed of weak Bragg features, the pattern observed by magnetic polarized neutron diffraction is beyond reasonable doubt. The result is a cautionary note on a subtraction of Bragg diffraction patterns obtained for high and low temperature modifications of a sample to estimate the magnetic signal. Its use in earlier studies of  $5d^2$  double perovskites returned null results for magnetic Bragg spots [18–21]. The inferred magnetic crystal class for  $\text{Ba}_2\text{YReO}_6$  is  $mmm1'$  (no. 8.2.25) that contains all inversions ( $\bar{1}$ ,  $1'$ ,  $\bar{1}'$ ), and any kind of magnetoelectric (ME) effect is prohibited. Magnetic dipoles, depicted in Fig. 1, possess an antiferromagnetic, noncollinear motif represented by space group  $P_{ccn}$  (no. 56.375, BNS setting [22]) involving two arms of the star  $\{(1, 0, 0) \text{ and } (0, 0, 1)\}$ .

A wave function for the ground state of rhenium  $5d^2$  compatible with symmetry uses five independent coefficients, and we report corresponding multipoles from dipole to hexadecapole. We propose a minimal model with just two coefficients; one measures the orientation of magnetic dipoles, and the second is a mixing angle for nonmagnetic and magnetic crystal-field states. The model can be tested

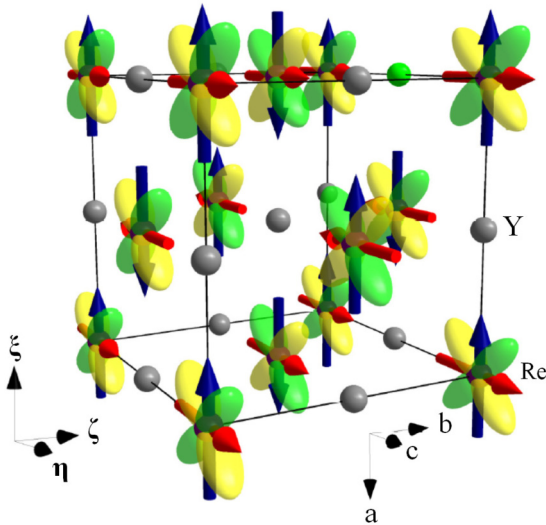


FIG. 1. Rhenium magnetic dipoles in the  $\xi$ - $\eta$  plane (components red and blue arrows) and chargelike quadrupoles  $\propto \xi\eta$  in  $\text{Ba}_2\text{YReO}_6$  using space group  $P_{Cccn}$  (no. 56.375). Grey spheres represent Y ions.

by confronting it with more knowledge on the primary magnetic order parameter, and, critically, missing knowledge about chargelike quadrupoles that are likely a secondary order parameter. Indeed, symmetry-allowed magnetoelastic coupling creates TT scattering. The diagonal component of the quadrupole is a function of the mixing angle alone, and a nonzero hexadecapole contradicts our minimal model. Resonance enhanced single-crystal Bragg diffraction of x rays can test all aforementioned features of chargelike multipoles, for which we report relevant scattering amplitudes. The diffraction technique can also provide the orientation of magnetic dipoles, as in a previous example using an iridate [23]. Concerning neutron Bragg diffraction, even rank multipoles that result from dyadic correlations of the anapole and position operators are absent in our calculations, because crystal-field states for the atomic configuration  $d^2$  in an octahedral environment belong to a  $J$  manifold. This is unlike an iridium ion in  $\text{Sr}_2\text{IrO}_4$ , for which there is more than one  $J$  manifold in crystal-field states and even rank multipoles are permitted [15].

## II. MATERIAL PROPERTIES

Two broad anomalies at temperatures  $\approx 50$  and  $\approx 25$  K are evident in the specific heat of  $\text{Ba}_2\text{YReO}_6$  as is the absence of a sharp lambda peak, which would signal long-range magnetic order [18]. The parent double perovskite crystal structure is composed of rocksalt ordered, corner-shared octahedra. Rhenium ions are in centrosymmetric sites with symmetry  $m\bar{3}m$ , namely, sites (4a) (0, 0, 0) in  $Fm\bar{3}m$  (no. 225), and Re chargelike hexadecapoles are permitted, with lattice constant  $\approx 8.3628$  Å [18,20]. Miller indices for the parent structure satisfy  $F$  centering with  $H_o + L_o$ ,  $K_o + L_o$ ,  $H_o + K_o$  simultaneously even. For the most part, we use the magnetic space group  $P_{Cccn}$  in which Re ions occupy centrosymmetric sites (4e) with symmetry,  $2'/m'$  that forbids a dipole moment parallel to the crystal  $b$  axis. ME and piezomag-

netic effects are absent, and Dirac multipoles are forbidden. Local rhenium coordinates are denoted  $(\xi, \eta, \zeta)$  with  $\xi = [-1, 0, 0]$ ,  $\eta = [0, 0, 1]$ ,  $\zeta = [0, 1, 0]$  and integer Miller indices  $h = -H_o$ ,  $k = L_o$ , and  $l = K_o$ .

The high-spin state of the  $\text{Re}^{5+}$  ( $5d^2$ ) is  ${}^3F$ . Spin-orbit coupling is proportional to  $Z^4$ , where  $Z$  is the atomic number, and atomic states of the rhenium ion are assumed to be those of the total angular momentum  $J$ . The value of the spin-orbit coupling is likely to be lower than the free-ion value, because of bonding effects known to reduce the observed magnetic moment in antiferromagnetic structures [24].

Crystal-field states for the atomic configuration  $5d^2$  in an octahedral environment are well established [25–28]. The crystal field is diagonalized before the Coulomb interaction, which is assumed large compared to the spin-orbit coupling. In octahedral symmetry, the ground state comprises three  $d$ -electron states labeled  $t_2$ , which take part in  $\pi$  bonding with ligand ions. Irrespective of the balance between the strengths of spin coupling and crystal field, the ground state of two electrons possesses a total spin  $S = 1$  and threefold orbital multiplicity. Adding spin-orbit coupling leads to a ground state denoted  ${}^3P_2$  in Ref. [28], with a total angular momentum  $J = 2$  formed from  $S = 1$  and a fictitious angular momentum  $=1$  representing the orbital triplet [25]. The ground state is composed of a doublet ( $\Gamma_3$  or  $E$  level) with magnetic projections  $M = 0, \pm 2$ , and a triplet ( $\Gamma_5$  or  $T_2$ ) with projections  $M = \pm 1, \pm 2$ . Specifically,

$$\begin{aligned} |\Gamma_3\rangle &= |0\rangle, \quad (1/\sqrt{2})[|+2\rangle + |-2\rangle]; \\ |\Gamma_5\rangle &= |+1\rangle, |-1\rangle, (1/\sqrt{2})[|+2\rangle - |-2\rangle], \end{aligned} \quad (1)$$

where  $|M\rangle = |J = 2, M\rangle$ . The double direct product  $\Gamma_3 \times \Gamma_3$  of the cubic group does not contain  $\Gamma_4(T_1)$ . Thus, a dipole operator has vanishing matrix elements in the  $\Gamma_3$  manifold, and the doublet is nonmagnetic. On the other hand, the direct product  $\Gamma_3 \times \Gamma_5$  contains  $\Gamma_4$  once and nonvanishing matrix elements of a dipole between the two manifolds may exist [25].

## III. MULTIPOLES AND MINIMAL MODEL

Our ground-state wave function Eq. (2) is consistent with point-group symmetry in a magnetic space group inferred from a measured Bragg diffraction pattern, namely,  $P_{Cccn}$  (no. 56.375) with Re ions using sites (4e). There are a large number of parameters in Eq. (2), likely too many to be reliably inferred from experiments. We derive all multipoles allowed by Eq. (2) to facilitate a test against experimental data at some future date. In the meantime, the number of parameters is pared down, in the spirit of Ockhams' razor, to a minimal model. Paring down is not a random process, but one motivated by consequences. And, indeed, we show that one retained parameter measures the orientation of axial dipoles, which remains to be tested. A second, mixing parameter furnishes nonzero values for the measured magnetic dipole moment through violation of time-reversal symmetry, i.e., its presence in the minimal model is justified by observations. Analysis at the mean-field level of a feasible model of the atomic configuration  $d^2$  by Chen and Balents [17,29] yields specific supporting evidence.

Axial (parity-even) multipoles of integer rank  $K$  are denoted  $\langle T_Q^K \rangle$ , where projections  $Q$  obey  $-K \leq Q \leq K$ , and angular brackets  $\langle \dots \rangle$  specify the time-average, or expectation, value of the enclosed spherical tensor operator. The property  $\langle T_Q^K \rangle^* = (-1)^Q \langle T_{-Q}^K \rangle$  yields  $\langle T_0^K \rangle$  purely real. All multipoles are time-odd for magnetic neutron scattering, of course, and the dipole  $\langle \mathbf{T}^1 \rangle$  is a linear combination of spin  $\langle \mathbf{S} \rangle$  and orbital  $\langle \mathbf{L} \rangle$  moments, to a good approximation. For x-ray Bragg diffraction enhanced by a parity-even atomic resonance the time signature of  $\langle T_Q^K \rangle$  depends on  $K$  alone, with  $K$  even (odd) charge-like (magnetic). In consequence, the time signature of multipoles  $\sigma_\theta = (-1)^K$  for magnetic neutron and resonance enhanced x-ray diffraction.

$$\begin{aligned} \langle T_\xi^1 \rangle &= \sqrt{(2/5)}(J||T^1||J)[\sqrt{(1/3)}(\alpha\gamma^*)' + \beta'\gamma'], & \langle T_\eta^1 \rangle &= -\sqrt{(2/5)}(J||T^1||J)[\sqrt{(1/3)}(\alpha\gamma^*)'' + \beta'\gamma''], \\ \langle T_0^2 \rangle &= \sqrt{(2/35)}(J||T^2||J)[|\alpha|^2 - |\beta|^2 - (1/2)|\gamma|^2], & \langle T_{+2}^2 \rangle &= \sqrt{(1/35)}(J||T^2||J)[2\alpha^*\beta' + (\sqrt{3}/2)(\gamma^*)^2], \\ \langle T_{+1}^3 \rangle &= \sqrt{(1/70)}(J||T^3||J)[- \sqrt{3}\alpha^*\gamma + 2\beta'\gamma^*], & \langle T_{+3}^3 \rangle &= -\sqrt{(1/14)}(J||T^3||J)\alpha^*\gamma^*, \\ \langle T_{+2}^4 \rangle &= (1/3)\sqrt{(1/7)}(J||T^4||J)[\sqrt{3}\alpha^*\beta' - (\gamma^*)^2], & \langle T_{+4}^4 \rangle &= (1/6)(\alpha^*)^2(J||T^4||J). \end{aligned} \quad (3)$$

Reduced matrix elements  $(J||T^K||J)$  for neutron and resonant x-ray diffraction are listed in the Appendix. Real and imaginary parts of a coefficient obey the phase convention  $\alpha = \alpha' + i\alpha''$  with  $\alpha'$  and  $\alpha''$  purely real. Notably,  $\alpha'$  and  $\beta$  specify  $\Gamma_3$  contributions, while  $\alpha''$  and  $\gamma$  specify  $\Gamma_5$  contributions. Multipoles of odd rank vanish for  $\gamma = 0$ . Magnetic dipole moments derived from  $\langle T_\xi^1 \rangle$  and  $\langle T_\eta^1 \rangle$  are

$$\begin{aligned} \mu_\xi &= \langle (L + 2S)_\xi \rangle = (4/3)[(\alpha\gamma^*)' + \sqrt{3}\beta'\gamma'], \\ \mu_\eta &= -(4/3)[(\alpha\gamma^*)'' + \sqrt{3}\beta'\gamma''], \end{aligned} \quad (4)$$

with  $\mu_\zeta = 0$  from symmetry.

A minimal model is achieved with  $\beta = 0$ ,  $\alpha = \cos(\chi)$ , and  $\gamma = \sin(\chi)\exp(i\phi)$ . Evidently, the model includes the singlet ground state of the crystal field potential  $[|+2\rangle + |-2\rangle]$  mixed with  $[|\gamma|+1\rangle + |\gamma^*|-1\rangle]$ , possibly by courtesy of a quadrupole force and opposing exchange forces [29]. Multipoles for the minimal model are labeled (a) and

$$\begin{aligned} \mu_\xi(a) &= \{(2/3) \sin(2\chi) \cos(\phi)\}, \\ \mu_\eta(a) &= \{(2/3) \sin(2\chi) \sin(\phi)\}. \end{aligned} \quad (5)$$

These expressions reveal  $\phi$  as the orientation of the dipole in the  $\xi$ - $\eta$  plane.  $P_{CCcn}$  allows two orthogonal magnetic dipole components, along  $a$  and  $b$  directions of the magnetic space-group setting depicted in Fig. 1. A combination of the two components results in a noncollinear motif of dipoles, as mentioned in Sec. I. Both components are permitted different from zero and combined with any amplitudes, although one component might actually dominate with the second vanishingly small by comparison. Equation (5) defines a moment direction within the  $\xi$ - $\eta$  plane that, indeed, is compatible with  $P_{CCcn}$ .

Multipoles with odd rank vanish when the mixing angle  $\chi$  is set to zero. One finds

$$\langle T_\xi^1 \rangle_a = (3/2)\sqrt{(1/30)}(J||T^1||J)\mu_\xi,$$

Symmetry  $2'_\zeta$  at sites occupied by rhenium ions means that multipole rank and projection obey  $K + Q$  even for all  $K$ , i.e.,  $\langle T_0^K \rangle = 0$  for  $K$  odd. Saturation values of multipoles  $\langle T_Q^K \rangle = \langle g|T_Q^K|g \rangle$  are derived using a ground-state wave function,

$$\begin{aligned} |g\rangle &= \beta|0\rangle + (1/\sqrt{2})[\alpha|+2\rangle + \alpha^*|-2\rangle] \\ &+ (1/\sqrt{2})[\gamma|+1\rangle + \gamma^*|-1\rangle], \end{aligned} \quad (2)$$

and coefficients  $\{|\alpha|^2 + |\beta|^2 + |\gamma|^2\} = 1$  for normalization. The time-reversal operator changes the sign of  $[|\gamma|+1\rangle + \gamma^*|-1\rangle]$  and  $[|+2\rangle - |-2\rangle]$  that transform as  $\Gamma_5$ . We find

$$\begin{aligned} \langle T_\eta^1 \rangle_a &= (3/2)\sqrt{(1/30)}(J||T^1||J)\mu_\eta, \\ \langle T_{+1}^3 \rangle_a &= -(3/4)\sqrt{(3/70)}(J||T^3||J)(\mu_\xi + i\mu_\eta), \\ \langle T_{+3}^3 \rangle_a &= -(3/4)\sqrt{(1/14)}(J||T^3||J)(\mu_\xi - i\mu_\eta), \\ \langle T_0^2 \rangle_a &= \sqrt{(1/70)}(J||T^2||J)[3\cos^2(\chi) - 1], \\ \langle T_{+2}^2 \rangle_a &= (1/2)\sqrt{(3/35)}(J||T^2||J)\sin^2(\chi)\exp(-2i\phi). \end{aligned} \quad (6)$$

Hexadecapoles  $\langle T_{+2}^4 \rangle$  and  $\langle T_{+4}^4 \rangle$  are proportional to  $(\gamma^*)^2$  and  $\cos^2(\chi)$ , respectively. The result for  $\langle T_0^2 \rangle_a$  gives additional meaning to  $\chi$ . An observed magnetic moment  $\mu_o = \{(2/3)|\sin(2\chi)|\} \approx 0.29$  in units of  $\mu_B$  is consistent with  $\chi \approx 12.9^\circ$ , and  $[3\cos^2(\chi) - 1] \approx 1.85$  [17].

A second magnetic space group that belongs to the magnetic crystal class  $mmm1'$  is included in an analysis of the observed neutron Bragg diffraction pattern in terms of states in the Chen-Balents model [17,29].  $C_{Amca}$  (no. 64.480) describes a collinear antiferromagnetic structure involving one arm of the star. For this case, Re ions are in centrosymmetric sites (4a), and local coordinates  $(\xi, \eta, \zeta)$  are  $\xi = [-1, 0, 0]$ ,  $\eta = [0, -1, 0]$ ,  $\zeta = [0, 0, 1]$  with integer Miller indices  $h = -H_o$ ,  $k = -K_o$ , and  $l = L_o$ . Site symmetry  $mm'm'$  requires  $\sigma_\theta(-1)^Q = +1$ , and  $\langle T_Q^K \rangle = (-1)^K \langle T_{-Q}^K \rangle$ . In consequence, dipoles  $\langle T_\eta^1 \rangle = \langle T_\zeta^1 \rangle = 0$ , while  $\langle T_\xi^1 \rangle = -\sqrt{2}\langle T_{+1}^1 \rangle$ . Multipoles use  $\phi = 0$  in Eqs. (5) and (6) for the minimal model.

#### IV. MAGNETOELASTIC COUPLING

Magnetic space groups under consideration belong to the six-dimensional, time-odd  $mX^{5+}$  irreducible representation with the  $(0, 0; 0, \delta_4; \delta_5, 0)$  order parameter direction for the  $P_{CCcn}$  and  $(0, 0; 0, 0; \delta_5, 0)$  for the  $C_{Amca}$  [17]. As already mentioned,  $P_{CCcn}$  involves two arms of the star  $\{(1, 0, 0)$  and  $(0, 0, 1)\}$ . There is a trilinear free-energy invariant that couples  $mX^{5+}$  with the time-even representation  $X^{4+}(\rho; 0; 0)$

associated with the third arm (0, 1, 0),  $\rho\delta_4\delta_5$ . In consequence, diffraction created by time-even multipoles violating  $F$  centering is permitted, e.g.,  $k+l$  odd. A specific example of this type of space-group forbidden diffraction is presented in Sec. VI.

The  $X^{4+}$  representation does not enter into mechanical decomposition of the reducible representation associated with the Re site in  $Fm\bar{3}m$ . This means that the magnetoelastic coupling does not couple the relevant Re displacements with this symmetry and, therefore, only higher order Re multipoles will be responsible for the scattering at space-group forbidden reflections (TT scattering). On the other hand, the  $X^{4+}$  representation does appear in the decomposition of the mechanical reducible representation associated with oxygen positions. This result implies that the magnetoelastic coupling will move oxygen ions in such a way that normal Thomson scattering will appear in the positions forbidden by the  $F$  centering, and oxygen displacements have the propagation vector (0, 1, 0).

## V. NEUTRON DIFFRACTION

Environments at sites (0, 0, 0) and (1/2, 0, 1/2) in  $P_Cccn$  are related by a dyad  $2_\xi$ , and  $2_\xi\langle T_Q^K \rangle = (-1)^K\langle T_{-Q}^K \rangle$ . The electronic structure factor for diffraction is  $\Psi_Q^K = [\exp(i\boldsymbol{\kappa} \cdot \mathbf{d})\langle T_Q^K \rangle_{\mathbf{d}}]$ , where the Bragg wave vector  $\boldsymbol{\kappa} = (h, k, l)$ , and the implied sum is over four rhenium sites in a unit cell. One finds

$$\Psi_Q^K(56.375) = [1 + \sigma_\theta(-1)^{h+k}][\langle T_Q^K \rangle + (-1)^{h+l}(-1)^K\langle T_{-Q}^K \rangle] \quad (7)$$

with  $\sigma_\theta = -1$  for magnetic neutron scattering. Bulk magnetization is zero, as expected. The selection rule  $h+k$  odd from antitranslation violates  $F$  centering, and there is no nuclear scattering. The amplitude for magnetic neutron diffraction  $\langle \mathbf{Q}_\perp \rangle$  is readily obtained from standard expressions, e.g.,  $K = 1$  and 3 in Eqs. (6.2)–(6.4) in Ref. [30]. With  $h+k$  odd, leading-order contributions to the intermediate magnetic scattering amplitude in  $\langle \mathbf{Q}_\perp \rangle = \{\mathbf{p} \times (\langle \mathbf{Q} \rangle \times \mathbf{p})\}$  are

$$\begin{aligned} h+l \text{ even; } \langle Q_\xi \rangle &\approx 6\langle T_\xi^1 \rangle \\ \langle Q_\eta \rangle &\approx \sqrt{21}p_\xi p_\eta [\sqrt{15}\langle T_{+3}^3 \rangle' + \langle T_{+1}^3 \rangle'], \\ \langle Q_\zeta \rangle &\approx -4\sqrt{21}p_\xi p_\zeta \langle T_{+1}^3 \rangle', \\ h+l \text{ odd: } \langle Q_\xi \rangle &\approx -\sqrt{21}p_\xi p_\eta [\sqrt{15}\langle T_{+3}^3 \rangle'' - \langle T_{+1}^3 \rangle''], \\ \langle Q_\eta \rangle &\approx 6\langle T_\eta^1 \rangle, \quad \langle Q_\zeta \rangle \approx -4\sqrt{21}p_\eta p_\zeta \langle T_{+1}^3 \rangle'', \end{aligned} \quad (8)$$

where the unit vector  $\mathbf{p} = (\kappa_\xi, \kappa_\eta, \kappa_\zeta)/\kappa$ .

Diffraction from a powder sample has an intensity

$$I = \sum_{\kappa, Q} [3/(K+1)] |\langle T_Q^K \rangle|^2, \quad (9)$$

in the absence of even rank multipoles. In the present case,  $K = 1$  and 3, and  $Q = \pm 1, \pm 3$ . Intensity derived from Eq. (6) for the minimal model,

$$I(a) = (1/6)\mu_o^2 \{d(\kappa) + 0.170[\langle j_2(\kappa) \rangle + (10/3)\langle j_4(\kappa) \rangle]^2\} \quad (10)$$

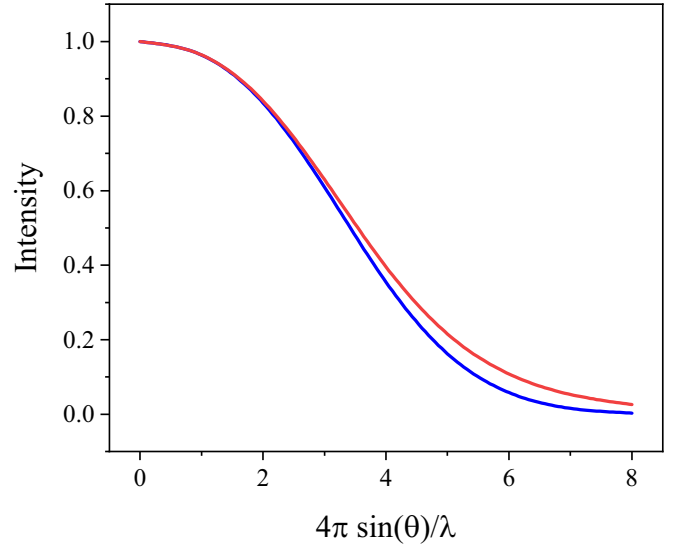


FIG. 2. Powder intensity Eq. (10) for the minimal model is displayed as a function of  $\kappa = \{4\pi \sin(\theta)/\lambda\}$ , where  $\theta$  is the Bragg angle in Fig. 3, in the range  $0-8 \text{ \AA}^{-1}$  using  $[(1/6)\mu_o^2]$  as a unit of intensity. Blue curve: dipole intensity  $d(\kappa) = [\langle j_0(\kappa) \rangle + (76/35)\langle j_2(\kappa) \rangle]^2$ . Red curve: dipole plus octupole contributions with  $K = 3$ ,  $Q = \pm 1, \pm 3$ . Radial integrals for  $\text{Re}^{5+} (5d^2)$  from Kobayashi *et al.* [30].

with dipole intensity  $d(\kappa) = [\langle j_0(\kappa) \rangle + (76/35)\langle j_2(\kappa) \rangle]^2$ , displayed in Fig. 2, together with  $I(a)$ . Radial integrals  $\langle j_n(\kappa) \rangle$  for  $\text{Re}^{5+} ({}^3F_2)$  are taken from Ref. [31]. In the so-called dipole approximation for  $d(\kappa)$  the coefficient of  $\langle j_2(\kappa) \rangle$  is replaced by  $(2-g)/g = 2$ , where the Landé splitting factor  $g = 2/3$  [30]. For observed Bragg spots [17]

$$\begin{aligned} (1, 0, 0)\kappa &\approx 0.7513 \text{ \AA}^{-1}, \quad \langle j_0(\kappa) \rangle^2 = 0.8689(0.9801), \\ I(a) &= 0.9802, \\ (1, 0, 1)\kappa &\approx 1.0625 \text{ \AA}^{-1}, \quad \langle j_0(\kappa) \rangle^2 = 0.7546(0.9589), \\ I(a) &= 0.9594, \\ (1, 0, 2)\kappa &\approx 1.6800 \text{ \AA}^{-1}, \quad \langle j_0(\kappa) \rangle^2 = 0.4913(0.8883), \\ I(a) &= 0.8913, \end{aligned} \quad (11)$$

with  $I(a)$  in units of  $(1/6)\mu_o^2$ , and values of  $d(\kappa)$  are given in brackets. There is next to no difference between  $d(\kappa)$  and  $I(a)$ , which includes octupoles, in the range of  $\kappa$  covered in the available diffraction pattern [17]. Returning to Fig. 2, the contribution from octupoles to scattering is discernible beyond  $\kappa \sim 4 \text{ \AA}^{-1}$ .

## VI. RESONANCE ENHANCED X-RAY DIFFRACTION

Parity-even absorption events are the only ones allowed for rhenium ions in  $P_Cccn$ . Dipoles and quadrupoles contribute to x-ray Bragg diffraction enhanced by an electric dipole–electric dipole ( $E1-E1$ ) event, while the octupole and hexadecapole are additions to an electric quadrupole–electric quadrupole ( $E2-E2$ ) event. Absorption at Re  $L$  edges access multipoles formed with 5  $d$  states ( $L_2$  edge  $\approx 11.95 \text{ keV}$ ,  $L_3 \approx 10.53 \text{ keV}$ ). Calculated dipole strengths



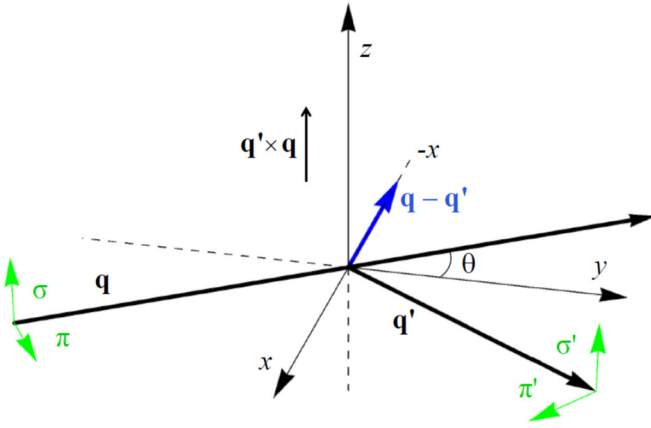


FIG. 3. X-ray diffraction. Primary ( $\sigma$ ,  $\pi$ ) and secondary ( $\sigma'$ ,  $\pi'$ ) states of polarization. Corresponding wave vectors  $\mathbf{q}$  and  $\mathbf{q}'$  subtend an angle  $2\theta$ . Local rhenium axes ( $\xi$ ,  $\eta$ ,  $\zeta$ ) and depicted Cartesian coordinates ( $x$ ,  $y$ ,  $z$ ) coincide in the nominal setting of the crystal.

$[(3p|R|5d)/\langle 2p|R|5d \rangle] \approx 3.3$  imply that diffraction intensity is an order of magnitude larger at  $M_3 \approx 2.45$  keV [32]. Unlike neutron diffraction, our x-ray multipoles do not depend on the magnitude of the scattering vector, although the  $E2$ - $E2$  amplitude is proportional to the square of the photon energy. Absorption at rhenium  $s$ -state edges include the  $K$  edge  $\approx 71.67$  keV and  $L_1$  edge  $\approx 12.52$  keV, and amplitudes have relative values  $\sim \{[\langle 2s|R^2|5d \rangle_{E_{L1}}]/[\langle 1s|R^2|5d \rangle_{E_K}]\}^2 \approx 0.3$ .

In the general case, x-ray multipoles  $\langle t_Q^K \rangle$  are calculated using Eq. (3) and reduced matrix elements in the Appendix. Celebrated sum rules include  $[\langle \mathbf{t}^1 \rangle_{L2} + \langle \mathbf{t}^1 \rangle_{L3}] = -\langle \mathbf{L} \rangle / (10\sqrt{2})$  [33]. Explicit results for the minimal model used throughout this section are derived from Eq. (6). Diffraction amplitudes are calculated with the electronic structure factor (7). Amplitudes in the rotated  $E1$ - $E1$  channel of photon polarization, labeled  $\pi'\sigma$  in the standard notation used in Fig. 3 [34], access magnetic dipoles and charge-like quadrupoles, while dipoles are absent in the unrotated  $\sigma'\sigma$  channel. For Bragg spots  $\kappa = (h, 0, 0)$  and enhancement at the  $L_2$  edge,  $\langle t_\eta^1(11) \rangle_{L2} = -\{[26/(225\sqrt{2})]\mu_\eta\}$  for  $h$  odd, while for  $h$  even scattering is by the real part of quadrupoles, including  $\langle t_0^2(11) \rangle_{L2} = \{[8/(525\sqrt{6})][3\cos^2(\chi) - 1]\}$ . Corresponding multipoles at the  $L_3$  edge are obtained by simple multiplication by fractions (19/26) or  $-(13/4)$  for dipole and quadrupole, respectively, and the cited dipole sum rule is readily confirmed. Different magnetic information is derived from Bragg spots indexed by  $(0, k, 0)$ . Specifically, the dipole  $\langle t_\xi^1(11) \rangle$  is for  $k$  odd, while charge-like scattering is also by the real part of quadrupoles. In summary, measurements of Bragg spots indexed by  $(h, 0, 0)$  and  $(0, k, 0)$  have the potential to deliver the orientation of dipole moments in the  $\xi$ - $\eta$  plane and the  $\Gamma_3$ - $\Gamma_5$  mixing angle.

All Bragg spots indexed by  $(0, 0, l)$  arise from charge-like multipoles. Space-group forbidden TT scattering that occurs for  $l$  odd is created by purely imaginary multipoles with rank  $K = 2$  and 4. For this case, and enhancement by an  $E1$ - $E1$  absorption event, the amplitude in the rotated channel

of diffraction is

$$F_{\pi'\sigma}(11) = -4 \sin(\theta) \cos(2\psi) \langle t_{+2}^2(11) \rangle'''. \quad (12)$$

Here,  $\psi$  is the angle of rotation of the crystal about the Bragg wave vector, and the origin of the azimuthal-angle scan places the  $\xi$  axis normal to the plane of scattering. Primary and secondary x-ray beams subtend an angle  $2\theta$  as in Fig. 3. Continuing with our use of the minimal model,  $\langle t_{+2}^2(11) \rangle_{L2}'' = -(3/350)[(\mu_\xi\mu_\eta)/\cos^2(\chi)]$ . The amplitude for diffraction enhanced by an  $E2$ - $E2$  event,  $K$  or  $L_1$  edge, is similar,

$$F_{\pi'\sigma}(22) = 2\sqrt{(1/7)} \cos(2\psi) [\sqrt{3} \sin(3\theta) \langle t_{+2}^2(22) \rangle'' + \sin(\theta) \{1 + \sin^2(\theta)\} \langle t_{+2}^4(22) \rangle'' + 2 \sin(\theta) \cos^2(\theta) \cos(4\psi) \langle t_{+4}^4(22) \rangle'']. \quad (13)$$

This diffraction is an analog of observations reported by Finkelstein *et al.* for haematite [2,35]. Intensities measure the orbital angular momentum content of the  $d$  shell, since the  $s$ -like core state is not split by the spin-orbit interaction [36]. As for numerical values in our minimal model, we find  $\langle t_{+2}^2(22) \rangle'' = -(9/2)\sqrt{(3/7)} \langle t_{+2}^2(11) \rangle_{L2}''$ ,  $\langle t_{+2}^4(22) \rangle'' = -(55/4)\sqrt{(1/7)} \langle t_{+2}^4(11) \rangle_{L2}''$ , and  $\langle t_{+4}^4(22) \rangle'' = 0$ . In consequence, diffraction enhanced by an  $E2$ - $E2$  event is a straightforward test of the model.

## VII. CONCLUSIONS

In summary, we have demonstrated that the small ordered magnetic dipole moment observed in a recent neutron diffraction experiment on  $\text{Ba}_2\text{YReO}_6$  implies significant multipolar moments [17]. These arise from a combination of the spin-orbit coupled  $J = 2$  ground state and the  $P_{CCcn}$  space group symmetry of the dipole ordered low-temperature state. The contribution of each multipole may be estimated by considering a minimal model for the ground state wave function that includes the mixing between the  $\Gamma_3$  and  $\Gamma_5$  states and the dipole moment direction as parameters inferred from experimental data. When the experimental ordered dipole moment is inserted into the corresponding model expectation value, it is found that the dominant multipolar component is the charge-like quadrupole, albeit with significant contributions up to the hexadecapole. Quadrupoles in a  $J$  manifold do not contribute to magnetic neutron diffraction, and magnetic scattering from octupoles is peaked at large scattering wave vectors  $\kappa$ , illustrated in Fig. 2, which together explain why no evidence of either is observed in existing neutron data. As such, the likely underlying multipolar orders in  $\text{Ba}_2\text{YReO}_6$  must be probed by renewed neutron diffraction investigations or other means; resonance-enhanced x-ray diffraction at the Re  $L$  edge is sensitive to both dipoles and quadrupoles through  $E1$ - $E1$  and octupoles and hexadecapoles through  $E2$ - $E2$  events. These experiments must, however, await the growth of single crystals.

## APPENDIX

Here we present the reduced matrix elements used in text. First is the neutron diffraction [30],

$$\begin{aligned} \langle J || T^1 || J \rangle &= (2/3)\sqrt{(10/3)}[\langle j_0(\kappa) \rangle + (76/35)\langle j_2(\kappa) \rangle], \\ \langle J || T^3 || J \rangle &= -(6/7)\sqrt{(2/5)}[\langle j_2(\kappa) \rangle + (10/3)\langle j_4(\kappa) \rangle], \end{aligned} \quad (\text{A1})$$

with  $\kappa = \{(4\pi/\lambda) \sin(\theta)\}$ , where  $\theta$  is the Bragg angle displayed in Fig. 3 and  $\lambda$  is the wavelength. Radial integrals are defined such that  $\langle j_0(0) \rangle = 1$ , and  $\langle j_n(0) \rangle = 0$  for  $n \geq 2$ .

Turning to resonance enhanced x-ray diffraction [34],

$$\begin{aligned} [J||t^1(11)||J]_{L_2} &= -(52/45)\sqrt{(1/15)}, & [J||t^1(11)||J]_{L_3} &= -(38/45)\sqrt{(1/15)}, \\ [J||t^2(11)||J]_{L_2} &= (8/15)\sqrt{(1/105)}, & [J||t^2(11)||J]_{L_3} &= -(26/15)\sqrt{(1/105)}. \end{aligned} \quad (\text{A2})$$

Last, for  $E2$ - $E2$  reduced matrix elements ( $ns$  edge, valence  $d$  state) we use [34]

$$\begin{aligned} [J||t^K(22)||J] &= (1/5)\sqrt{[2(2K+1)](-1)^K} W^{(0K)K}, \\ W^{(0K)K} &= (2J+1) \begin{Bmatrix} S & S & O \\ L & L & K \\ J & J & K \end{Bmatrix} W^{(0K)} \quad \text{with } W^{(0K)} = \sqrt{[(1/2)(2S+1)]} V(K), \end{aligned}$$

where the Racah unit tensor  $V(K)$  is tabulated in Ref. [35]. For the atomic configuration  $^3F_2$ ,

$$\begin{aligned} [J||t^1(22)||J] &= -(4/5)\sqrt{(1/3)}, & [J||t^2(22)||J] &= -(12/35)\sqrt{(1/5)}, \\ [J||t^3(22)||J] &= (3/5)\sqrt{(1/7)}, & [J||t^4(22)||J] &= (11/35). \end{aligned} \quad (\text{A3})$$

- 
- [1] D. H. Templeton and L. K. Templeton, *Acta Crystallogr., Sect. A* **42**, 478 (1986).
- [2] K. D. Finkelstein, Q. Shen, and S. Shastri, *Phys. Rev. Lett.* **69**, 1612 (1992).
- [3] L. Paolasini C. Vettier, F. de Bergevin, F. Yakhou, D. Mannix, A. Stunault, W. Neubeck, M. Altarelli, M. Fabrizio, P. A. Metcalf, and J. M. Honig, *Phys. Rev. Lett.* **82**, 4719 (1999).
- [4] S. W. Lovesey and K. S. Knight, *J. Phys.: Condens. Matter* **12**, L367 (2020).
- [5] A. Rodríguez-Fernández, J. A. Blanco, S. W. Lovesey, V. Scagnoli, U. Staub, H. C. Walker, D. K. Shukla, and J. Stremper, *Phys. Rev. B* **88**, 094437 (2013).
- [6] S. W. Lovesey, J. Fernández-Rodríguez, J. A. Blanco, D. S. Sivia, K. S. Knight, and L. Paolasini, *Phys. Rev. B* **75**, 014409 (2007).
- [7] J. A. Paixão, C. Detlefs, M. J. Longfield, R. Caciuffo, P. Santini, N. Bernhoeft, J. Rebizant, and G. H. Lander, *Phys. Rev. Lett.* **89**, 187202 (2002).
- [8] M.-T. Suzuki, H. Ikeda, and P. M. Oppeneer, *J. Phys. Soc. Jpn.* **87**, 041008 (2018).
- [9] S. Ghosh, M. Matty, R. Baumbach, E. D. Bauer, K. A. Modic, A. Shekhter, J. A. Mydosh, E.-A. Kimand, and B. J. Ramshaw, *Sci. Adv.* **6**, eaaz4074 (2020).
- [10] C. G. Shull and J. S. Smart, *Phys. Rev.* **76**, 1256 (1949).
- [11] R. M. Moon, T. Riste, and W. C. Koehler, *Phys. Rev.* **181**, 920 (1969).
- [12] P. Bourges, Y. Sidis, and L. Mangin-Thro, *Phys. Rev. B* **98**, 016501 (2018).
- [13] J. Jeong, B. Lenz, A. Gukasov, X. Fabreges, A. Sazonov, V. Hutanu, A. Louat, D. Bounoua, C. Martins, S. Biermann, V. Brouet, Y. Sidis, and P. Bourges, *Phys. Rev. Lett.* **125**, 097202 (2020).
- [14] S. W. Lovesey, D. D. Khalyavin, and U. Staub, *J. Phys.: Condens. Matter* **27**, 292201 (2015); S. W. Lovesey and D. D. Khalyavin, *ibid.* **27**, 495601 (2015).
- [15] D. D. Khalyavin and S. W. Lovesey, *Phys. Rev. B* **100**, 224415 (2019).
- [16] T. Tiittanen, S. Vasala, and M. Karppinen, *Chem. Commun.* **55**, 1722 (2019).
- [17] G. J. Nilsen, C. M. Thompson, C. Marjerisson, D. I. Badrtdinov, A. A. Tsirlin, and J. E. Greedan, *Phys. Rev. B* **103**, 104430 (2021).
- [18] T. Aharen, J. E. Greedan, C. A. Bridges, A. A. Aczel, J. Rodriguez, G. MacDougall, G. M. Luke, V. K. Michaelis, S. Kroeker, C. R. Wiebe, H. Zhou, and L. M. D. Cranswick, *Phys. Rev. B* **81**, 064436 (2010).
- [19] C. M. Thompson *et al.*, *J. Phys.: Condens. Matter* **26**, 306003 (2014).
- [20] C. A. Marjerrison, C. M. Thompson, A. Z. Sharma, A. M. Hallas, M. N. Wilson, T. J. S. Munsie, R. Flacau, C. R. Wiebe, B. D. Gaulin, G. M. Luke, and J. E. Greedan, *Phys. Rev. B* **94**, 134429 (2016).
- [21] D. D. Maharaj, G. Sala, M. B. Stone, E. Kermarrec, C. Ritter, F. Fauth, C. A. Marjerrison, J. E. Greedan, A. Paramekanti, and B. D. Gaulin, *Phys. Rev. Lett.* **124**, 087206 (2020).
- [22] We use the BNS setting of magnetic space groups; see the Bilbao Crystallographic server, <http://www.cryst.ehu.es>.
- [23] L. C. Chapon and S. W. Lovesey, *J. Phys.: Condens. Matter* **23**, 252201 (2011).
- [24] J. Hubbard and W. Marshall, *Proc. Phys. Soc.* **86**, 561 (1965).
- [25] A. Abragam and B. Bleaney, *Electron Paramagnetic Resonance of Transition Ions* (Clarendon, Oxford, 1970).
- [26] M. Weissbluth, *Atoms and Molecules* (Academic, New York, 1978).
- [27] A. Georges, L. de' Medici, and J. Mravlje, *Annu. Rev. Condens. Matter Phys.* **4**, 137 (2013).
- [28] B. Yuan, J. P. Clancy, A. M. Cook, C. M. Thompson, J. Greedan, G. Cao, B. C. Jeon, T. W. Noh, M. H. Upton, D. Casa, T. Gog, A. Paramekanti, and Y.-J. Kim, *Phys. Rev. B* **95**, 235114 (2017).
- [29] G. Chen and L. Balents, *Phys. Rev. B* **84**, 094420 (2011).
- [30] S. W. Lovesey, *Phys. Scr.* **90**, 108011 (2015).
- [31] K. Kobayashi, T. Nagao, and M. Ito, *Acta Crystallogr., Sect. A* **67**, 473 (2011).

- [32] R. D. Cowan and R. D. Cowan, *The Theory of Atomic Structure and Spectra* (University of California Press, Berkeley, 1981).
- [33] B. T. Thole, P. Carra, F. Sette, and G. van der Laan, *Phys. Rev. Lett.* **68**, 1943 (1992); P. Carra, B. T. Thole, M. Altarelli, and X. D. Wang, *ibid.* **70**, 694 (1993); P. Carra, H. König, B. T. Thole, and M. Altarelli, *Physica B* **192**, 182 (1993).
- [34] S. W. Lovesey, E. Balcar, K. S. Knight and J. Fernández Rodríguez, *Phys. Rep.* **411**, 233 (2005); V. Scagnoli and S. W. Lovesey, *Phys. Rev. B* **79**, 035111 (2009).
- [35] P. Carra and B. T. Thole, *Rev. Mod. Phys.* **66**, 1509 (1994).
- [36] S. W. Lovesey, *J. Phys.: Condens. Matter* **10**, 2505 (1998).